

The *TRACE* Telescope Point Spread Function for the 171 Å filter

S. Gburek and J. Sylwester

*Space Research Centre, Polish Academy of Sciences, Solar Physics Division
Kopernika 11, 51-622 Wrocław, Poland*

P. Martens

Montana State University, PO Box 173840, Bozeman, MT 59717

Abstract. We perform an analysis of the *TRACE* telescope blur from EUV images. The blur pattern is discussed in terms of the telescope point spread function (PSF) for the 171 Å filter. The analysis performed consists of two steps. First an initial shape for the PSF core is determined directly from *TRACE* EUV images. Second, the blind deconvolution approach is used for obtaining the final PSF shape. The PSF core peak is fitted by analytical functions to determine its parametric characteristics. The determined PSF includes the core central peak and peaks caused by diffraction effects inherent in *TRACE* EUV data. The diffractive portion of the PSF is studied theoretically in Fraunhofer diffraction limit. The temperature dependence of the *TRACE* PSF shape is investigated for a selected temperature range. We also discuss a general properties of the obtained PSF and its possible applications.

Keywords: *TRACE*, PSF, Blind Deconvolution

1. Introduction

The Transition Region and Coronal Explorer (*TRACE*) satellite was launched from Vandenberg Air Force Base in USA on 2 April 1998 to perform observations of the solar photosphere, transition region and corona with high spatial resolution and temporal continuity. The satellite itself is a NASA Small Explorer (SMEX) spacecraft. The *TRACE* Sun-synchronous polar orbit allows for making uninterrupted solar phenomena observations except a few months lasting eclipse seasons when short sunsets take place. The *TRACE* satellite carries a 30 cm Cassegrain type telescope with a field of view of 8.5×8.5 arcmin and a spatial resolution of ~ 1 arcsec. The instrument multilayer optics focuses the solar radiation on CCD sensor of the size of 1024×1024 pixels (1 pixel = 0.5 arcsec).

The incident photon signal is converted into a charge within each CCD pixel and then represented by the instrument electronics in so called data numbers *DN*. The signal value measured in *DN*s is kept within the range 0 - 4095 *DN* with the saturation level of 4095 *DN*. *TRACE* observes solar plasma at a selected temperature range from



© 2006 Kluwer Academic Publishers. Printed in the Netherlands.

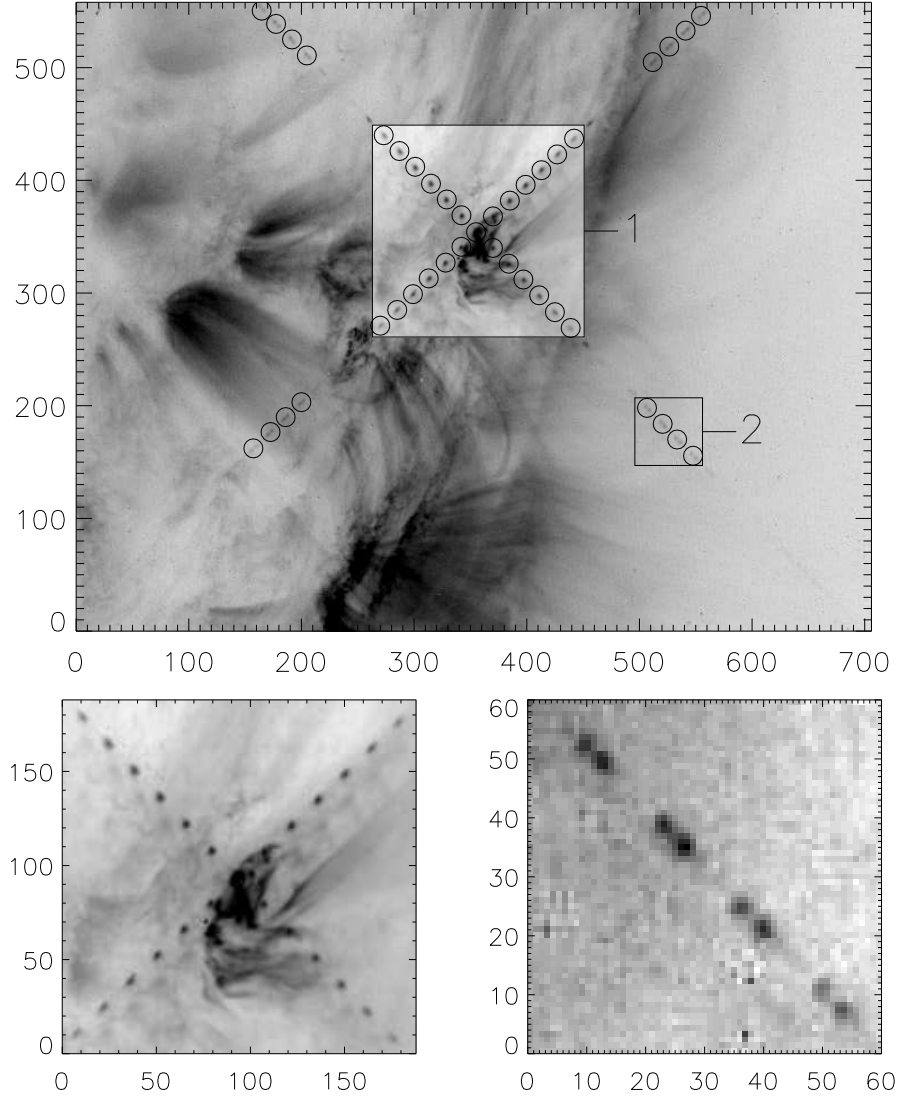


Figure 1. Top - *TRACE* 171 Å compact flare image taken on May 16, 1999 at 13:49:22 UT with an exposure time of 19.5 s. The *TRACE* PSF maxima are clearly visible extending outwards in four arms from the saturated flaring area. Encircled are the stronger maxima of orders 1-6 and 11-14 which are investigated in more detail in the present study. For presentation purposes different signal scaling was used for the image portion in the box 1) containing maxima up to sixth order. This portion is shown zoomed in the bottom - left panel. The subimage in the box 2) with further diffraction structures of orders 11-14 is zoomed in the bottom-right panel.

~ 6000 K for white light images up to ~ 20 MK for EUV ones with typical temporal resolution of less than 1 min. More details about the instrument can be found in (Handy et al., 1999). A review of *TRACE* early observations is given by Schrijver et al. (1999).

As any optical system, the *TRACE* telescope introduces a certain amount of blur to its images. This blurring pattern can be discussed in terms of the telescope point spread function (PSF) which describes the response of the entire optics to a distant point source. Unlike for many other recently flown high energy imaging systems, the *TRACE* PSF is not a single peaked function. Except the main central peak - the core caused by geometrical imperfectness of the optics, the *TRACE* PSF contain also other peaks which are formed as replications of the core due to diffraction on the nickel wire mesh supporting the telescope entrance filters.

2. *TRACE* PSF and diffraction pattern

The overall diffraction effects are particularly well observed in *TRACE* images of stronger compact sources, like the flaring kernels shown in Figure 1 and the top-left panels of Figures 2 and 3. The diffraction structures are spaced roughly every 20 pixels and arranged along two lines intersecting at an almost right angle.

The shape of the diffractive structure changes apparently with order. They are of the form of sharp well defined peaks only for the lowest six orders. For higher orders they get elongated and eventually split apart in double or multi-peaked structures. The overall signal intensity in the diffraction structures varies significantly with order. They fade out gradually and become invisible for the ninth order. For higher orders they brighten back and disappear again for order eighteen. In the images of stronger compact sources (Figure 1) the zeroth order structure and the lower order structures are often corrupted by saturation effects. The zeroth order structure and the structures up to sixth order are however well visible in non saturated *TRACE* images of relatively weak sources (see the top-left panels of Figure 2 and 3). From the inspection of data shown in Figure 1 and the top-left panels of Figures 2 and 3 it is seen that in non-saturated *TRACE* images of compact sources the diffraction extends up to the sixth order. The diffraction structures in such images has a form of sharp peaks. In saturated *TRACE* frames the diffraction is also seen in orders higher than sixth. In higher orders the diffraction structures become non uniformly shaped even if the observed source is compact. The shape variability of high order diffraction structures occurs due to large dispersion ef-

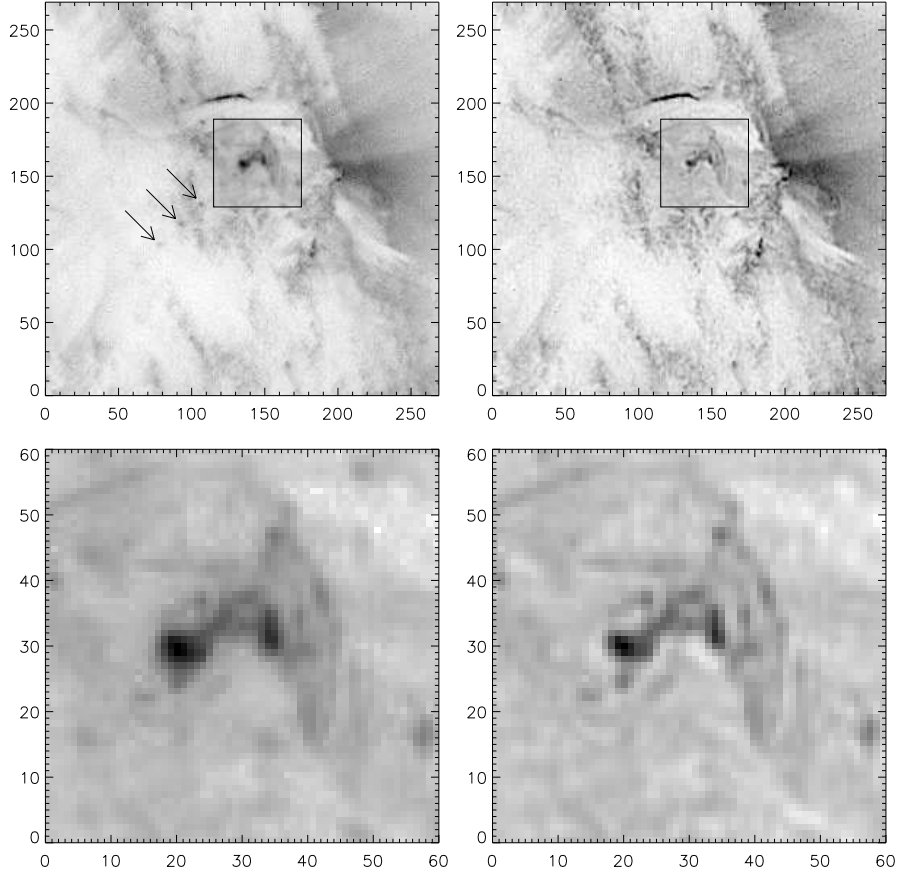


Figure 2. Top-left panel - a non-saturated image of compact EUV flaring event observed by *TRACE* in the 171 Å filter on 21 October 1999, at 19:54:43 UT with an exposure time of 5 s. The diffraction effects are visible up to sixth order in this image (three of the diffraction structures seen in the lower-left pattern arm are pointed by arrows in the image). Top-right - deconvolved *TRACE* image corresponding to the image from the top-left panel. The central image portions (in the boxes) of both data and deconvolved frame are shown enlarged in the bottom-left and bottom-right panel respectively.

fects and source plasma conditions on which the incident spectrum is dependent.

The quantitative properties of the diffraction pattern seen in Figure 1 were determined in Lin, et al. (2001). We performed a similar analysis taking into account the brightest structures not corrupted by saturation seen in 1 - 6 and 11 - 14 diffraction orders. The analysis was performed for all four arms extending from the midpoint of the

whole diffraction pattern in Figure 1. For each analyzed structure we determined its support (the image area in which the structure signal exceeded three times the local noise level), subtracted background and calculated its position and intensity in the pattern coordinate system. We defined the structure position as an average position in its support weighted by signal value. Thus, the position (x_c, y_c) of each particular structure in image in Figure 1 reads:

$$(x_c, y_c) = \frac{1}{n} \sum (i, j) I(i, j), \quad (1)$$

in which pairs (i, j) label the image pixel coordinates, $I(i, j)$ is the signal value in DN in pixel (i, j) , n is a number of pixels in the neighborhood of the considered structure and the summation runs only over the particular neighborhood. Such defined positions exactly agree with peak positions for structures of orders 1 - 6. For the double peaked structures of higher orders (11 - 14) respective positions are placed somewhere near the midpoint between the peaks. The intensity of each structure was calculated as an integral of the background subtracted signal over the structure neighborhood.

We fitted two straight lines using linear regression to measure the geometry of the diffraction-cross seen in Figure 1. The first line was fitted to the determined structure positions from the lower-left and the upper-right arms of the pattern. The second line was fitted to the structure positions from the lower-right and the upper-left arms. In both cases a very good quality fit was obtained with a correlation coefficient of 0.99. From the fit parameters we calculated the angle between fitted straight lines and the horizontal bottom image edge. These angles are $\phi_1 = 44.02$ deg and $\phi_2 = 134.01$ deg (counterclockwise) for the first and the second fitted line respectively, so indeed the fitted lines are almost exactly orthogonal but do not run in parallel direction to CCD pixel diagonals (as it would be for $\phi_1 = 45$ deg and $\phi_2 = 135$ deg).

It has been checked in Lin, et al. (2001) and independently here that the structure intensity dependence on diffraction order can be explained well theoretically assuming the Fraunhofer diffraction limit for *TRACE* telescope. In this approach the structures seen in Figure 1 arise as principal maxima of the diffraction pattern produced by the two dimensional grating with square openings (Lin, et al., 2001). The theory also says that the principal maxima intensities can be related to the zeroth order peak intensity I_0 by the following expression

$$I_m = I_0 \left(\frac{\sin(m\pi\beta)}{m\pi\beta} \right)^2, \quad (2)$$

in which $m = 0, 1, 2, \dots$ is a diffraction order, I_m is the intensity of the m -th order maximum, β is a constant characteristic for the wire mesh

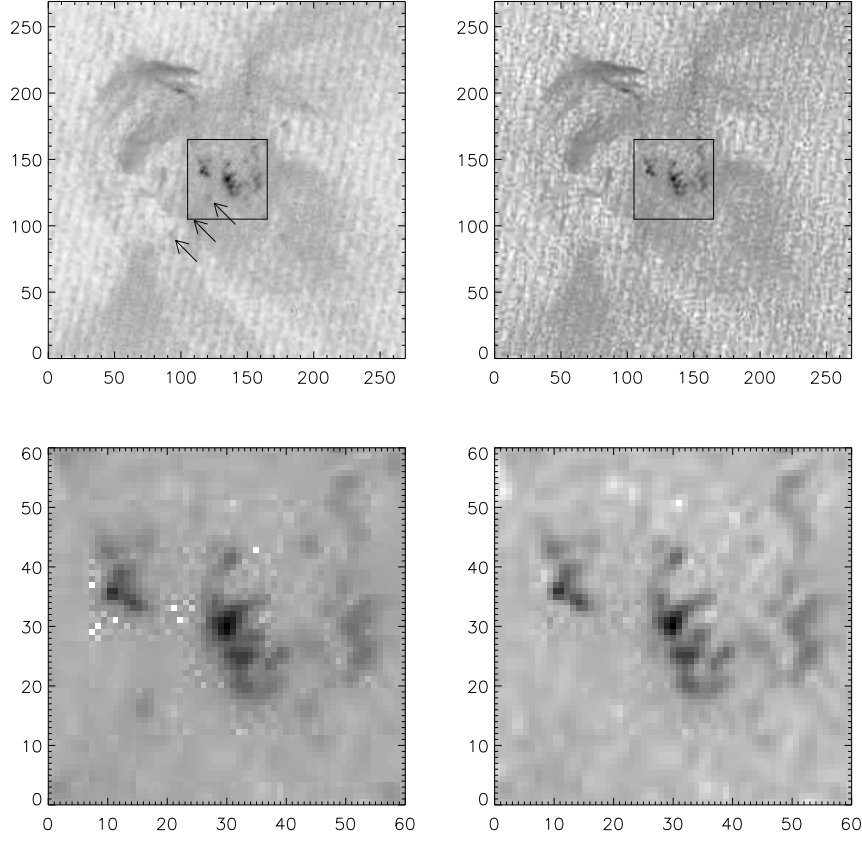


Figure 3. Top-left panel - a *TRACE* 171 Å compact flare image taken on Jun 19, 2001 at 09:56:46 UT with an exposure time of 1.0 s. The diffraction effects are visible up to sixth order in this image (three of the diffraction structures seen in the lower-left pattern arm are pointed by arrows in the image). This image after deconvolution is shown in the top-right panel. The central portion of both data and deconvolved image (in the boxes) are enlarged in the bottom-left and bottom right panel respectively.

geometry. It was calculated (Lin, et al., 2001) that for the *TRACE* entrance filter the mesh constant β equals 0.885.

Using the Fraunhofer theory of diffraction one can also derive an expression for the distance r_m of any principal maximum from the diffraction pattern center as a function of wavelength λ (Lin, et al., 2001). This expression reads:

$$r_m = m \frac{\lambda}{a}, \quad (3)$$

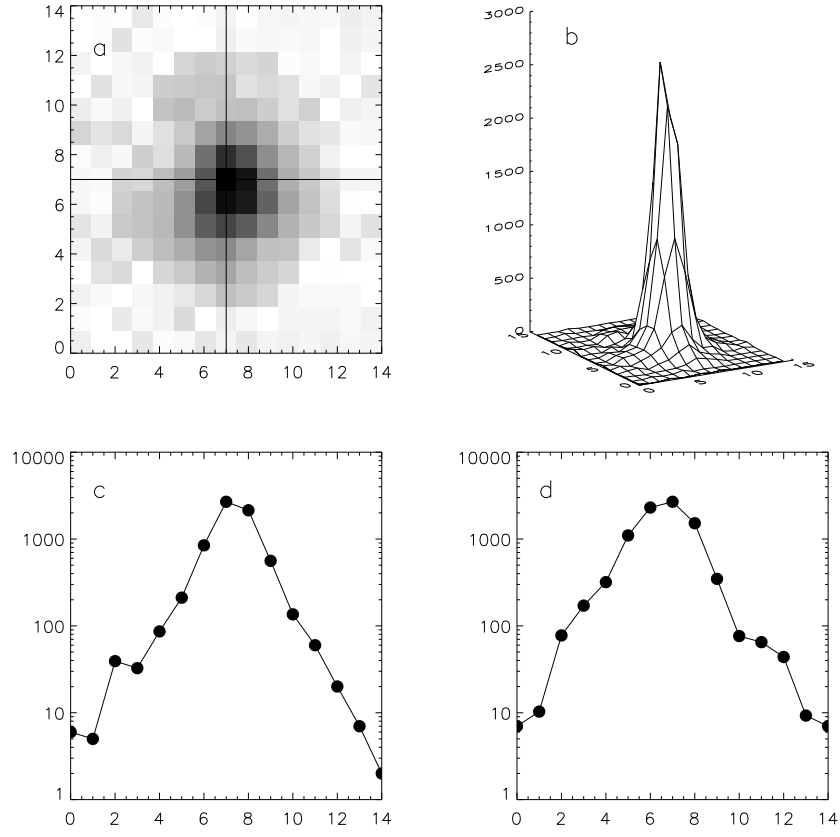


Figure 4. In panel (a) the enlarged image of the background subtracted first order maximum from the upper-left diffraction arm in Figure 1 is shown. In panel (b) a surface plot of data from (a) is shown. In panels (c) and (d) the cross sections of the maximum along the horizontal and vertical lines shown in (a) are plotted - thick solid line with black circles.

where m is the diffraction order, λ is the wavelength of incident radiation and a is the distance between wires of the mesh. For the *TRACE* telescope $a = 3.63 \times 10^{-4}$ m (Handy et al., 1999). For r_m in *TRACE* pixels and λ in Å the equation 2 takes the form:

$$r_m = 0.113804m\lambda. \quad (4)$$

The above discussed properties of the *TRACE* diffraction pattern allow for modeling the PSF provided that a spectrum of incoming radiation and PSF core are known. Modeling of the PSF for a given shape of illuminating spectrum consists of several steps. First the solar spectrum

has to be multiplied by the *TRACE* spectral response curve in order to take into account the overall attenuation introduced by the instrument. The next step is to redistribute spectral intensities over the CCD starting from a certain point chosen as the diffraction pattern center - the position of the zeroth order maximum. For proper redistribution one needs to determine diffraction maxima positions in the pattern by using equation 4 and angles ϕ_1, ϕ_2 . Scaling of the subordinate peak intensities is then obtained from equation 2. The redistribution procedure has to be repeated separately for each wavelength in the spectrum and summed together. Finally, the reconstructed diffraction pattern has to be convolved with the PSF core to account for instrument spatial blur and renormalized to unit integral. In principle it is possible to reconstruct the *TRACE* PSF up to arbitrary diffraction order in the way described above. In practice the PSF model is bounded by the CCD edges.

3. The core part of the *TRACE* PSF

Analysis of the *TRACE* telescope data as well as measuring telescope instrumental blur and diffraction effects requires the PSF core part to be well determined. From the general method for reconstruction of the entire *TRACE* PSF from a given EUV spectrum, described in the previous section, it follows that the core PSF peak constitute one of essential components in the reconstruction process. Hence, in this section, we discuss the PSF core properties, determine its shape and give its basic parametric characterization. In the previous publications concerning

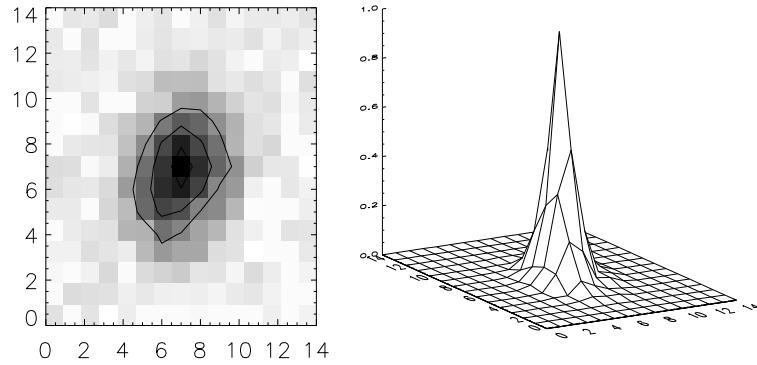


Figure 5. *TRACE* PSF core obtained by the SDM method.

the subject it was determined from analysis of the cross-sections of the thinnest loops observed in *TRACE* data (Watko & Klimchuk, 2000) that the *TRACE* PSF core full width at half maximum (FWHM) is about 2.5 pixels. The shape of the PSF core was also determined for the *TRACE* 171 Å channel using the blind iterative deconvolution (BID) approach (Golub et al., 1999). The obtained shape of deconvolved core was asymmetric, being elongated approximately at the position angle of 45 degrees. The upper limit of the core FWHM was found to vary within the range from about 2 to about 3 pixels with position angle. The azimuthal average of the core FWHM over position angle was 2.5 pixels.

Here, in order to obtain a first raw approximation of the PSF core we used the Steepest Descent Method (SDM) described in Gburek (2003). The final PSF core estimate was then also obtained by blind deconvolution of the *TRACE* image. The SDM method has been applied earlier for determination of the PSF core of the SXT telescope. This method takes for input a sequence of non-saturated images of compact narrow sources. Each image must be of the same fixed size and must have well defined signal maximum in the center pixel. The images in the input sequence are then normalized to the $[0, 1]$ signal range. Next the normalized sequence is searched for the lowest signal at any pixel position. The minimum values for each pixel are collected in a new array of the size of the sequence images. The new array gives the approximation of the PSF core. It has been found that good initial estimates of PSF cores can be obtained by the SDM method provided that a good quality image sequence had been chosen for the input. In particular it has been noted that the more compact sources are present in images from the input sequence the more accurate the PSF approximations obtained by the SDM method. Hence, we focused attention on the lowest six order diffraction peaks seen in Figure 1. All these peaks are quite narrow, especially the peaks of first and second order for which dispersion peak broadening is expected to be small. An example of a first order peak and its cross-sections are shown in Figure 4. To prepare the initial image sequence for the SDM method we took 15×15 pixel arrays centered at the peaks of low-order (up to sixth order), non-saturated, background subtracted, diffraction maxima seen in Figure 1. The diffraction peak sequence was next processed with the described above SDM method. Thus obtained approximation of the PSF core is shown in Figure 5. Its shape is a bit elongated roughly in the direction of the diagonal running from lower-left to upper-right corner of the image in Figure 5. The FWHM of the SDM determined core approximation as estimated by fitting 2D Gaussian profile has been found to be 2.5 pixels.

The SDM determined approximation of the PSF core was next used as the initial guess for blind deconvolution of *TRACE* images. It was performed here using the modified iterative algorithm described in Ayers, G. and Dainty (1998). The algorithm is based on a telescopic image formation model in which the relationship among observed count number in data is a pure convolution of the true brightness distribution of the imaged object with the PSF. The algorithm is particularly applicable to images with a high signal to noise ratio in which the noise contribution can be assumed to be insignificant. The BID method starts from a certain initial approximation for the PSF and performs iterative restoration of the true brightness distribution by improving the PSF and cleaning the image. The process of commutative restorations of the PSF and true brightness distribution is repeated until a convergence limit threshold is reached. As the algorithm convergence control criterion a value of the χ^2 parameter characterizing the difference between data and reconvolved image and PSF estimates at each iteration was calculated. The blind deconvolution iterations were stopped when the minimum of χ^2 parameter was found. Due to the noise in the data and the relative freedom in selection of the initial guess for the PSF (which, in general, is different from the real PSF) expected properties as non-negativity or conservation of the integral value of the flux are generally not preserved during BID processing. Hence, additional constraints were imposed on the recovered PSF and image estimates in order to conserve the characteristics known to be invariant at each iteration. Therefore, both estimates are forced to be positive, the PSF estimate is re-normalized to unit integral and the integral flux of the restored image is kept constant at each iteration.

The positivity of the image and PSF estimates were imposed using the same methods as described in detail in Ayers and Dainty 1988. During each iteration the re-normalization of the PSF estimate took place in the small areas surrounding PSF peaks. From the mentioned above SDM method of PSF determination we estimated that these areas contained more than 99 % of the entire PSF signal. Renormalization of the signal in image estimate was performed in the areas where data signal was greater than the noise level. The tests on the synthetic data showed that above 98 % of the flux in image can be restored using this method.

The tests performed using synthetic data revealed that the BID algorithm is capable of giving good restorations for both the image and the PSF. Trial deconvolutions on real and test data showed also that the performance and speed of the BID algorithm depend on the

initial guess for the shape of the PSF. After compatibility tests the deconvolution code will be integrated with the SolarSoft¹ environment.

As we deconvolved the non-saturated *TRACE* data shown in image in the top-left panels of Figures 2 and 3 we have had to prepare the initial PSF guess consisting of maxima up to sixth diffraction order. For the zeroth order maximum we took the core approximation obtained by the SDM method. For preparation of the initial guess for the remaining maxima one can use two methods. First, having the core approximation determined and the plasma parameters such as temperature and emission measure distribution known, at least for the brightest parts of the data to be deconvolved, one can generate the EUV spectrum of the observed solar radiation. Then the initial guess for the shape of higher order maxima can be modeled in the way described at the end of the previous section. On the other hand, for images of sources with well localized emission, like the one in the top-left panel of Figures 2 and 3, one can determine the initial shape of higher order diffraction peaks directly from the image. We decided to go for the second approach and prepared the initial approximation of diffraction maxima of order 1 – 6 from the background subtracted diffraction peaks shown in the top-left panels of Figures 1 and 2. The theoretical modeling of the *TRACE* PSF diffraction maxima in the isothermal approximation is discussed in the next section. The results of blind deconvolution are shown in Figure 6 and Figures 2 and 3.

In the deconvolved *TRACE* image there is a substantial increase in the signal range. The structures in the “clean” image are much sharper. The diffraction pattern was largely removed by deconvolution. No significant deformations of the image and PSF, which may come from noise or method artifacts, were detected. The value of χ^2 parameter (normalized per degrees of freedom number) at the last iteration of deconvolution process was 0.90 and 0.51 for the deconvolution of data shown in Figures 2 and 3 respectively. We fitted the elliptical Gaussian, Moffat and Voigt functions to the deconvolved PSF core in order to give it a parametric characterization. We used Fourier fitting methods which were previously applied for the PSF of the SXT telescope (Martens, Acton, & Lemen, 1995). This approach was found to be particularly useful for fitting spiky shapes such as the *TRACE* PSF core. We obtained the best quality of fit with the Moffat function. Voigt fits were also of good quality in the peak but too fuzzy in the off-peak core areas. The worst fit has been obtained using Gaussian function. The comparison of various fitting results are shown in Figure 7.

¹ <http://www.lmsal.com/solarsoft/>

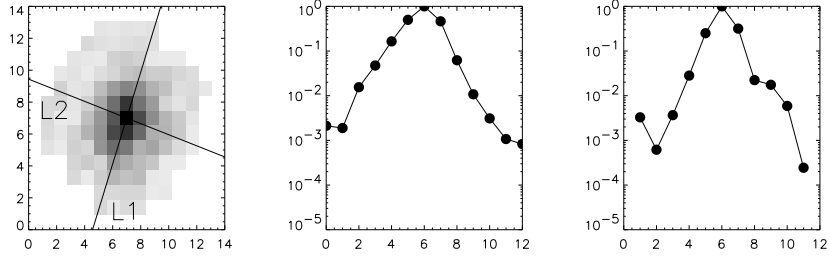


Figure 6. Deconvolved *TRACE* PSF core is shown in the left panel. In the middle and right panels the PSF core cross-sections along lines L1 and L2 are plotted.

Since quality of Moffat fit was the best we decided to use this function to give a parametric characteristic of the *TRACE* PSF core. The mathematical expression for the Moffat function that we used reads

$$f(r) = c \left(1 + \frac{r^2}{a^2} \right)^{-b} \quad (5)$$

in which r is the radial distance from the function peak - $r = \sqrt{x^2 + y^2}$ for planar Cartesian coordinates x, y , and a, b, c are parameters. This function defines a cylindrically symmetric surface in three-dimensional space with maximum value c and shape dependent on parameters a and b . To account for the observed elliptical deformations of the core the r variable in the equation 5 has been redefined as follows:

$$r^2 = x^2(1 + \sqrt{\varepsilon_x^2 + \varepsilon_y^2} - \varepsilon_x) + y^2(1 + \sqrt{\varepsilon_x^2 + \varepsilon_y^2} + \varepsilon_x) - 2\varepsilon_y xy. \quad (6)$$

Such a modification gives an elliptically deformed Moffat function with ellipticity determined by parameters ε_x , and ε_y . The two other parameters x_c and y_c were used for describing the offset of the fitting function peak position from the CCD pixel center. Hence x and y in equation 6 were actually redefined in the following way:

$$x = x - x_c, \quad y = y - y_c. \quad (7)$$

An additional parameter bg was introduced to represent background level. Hence, the form of the Moffat fitting function was fully described by eight parameters $(a, b, c, \varepsilon_x, \varepsilon_y, x_c, y_c, bg)$. The values of these parameters for the best fit are given in Table I. For Gaussian and Voigt fits we also allowed for elliptical deformations and off-center peak shift exactly in the same way as described above for Moffat function.

From the parameter values collected in Table I one can derive essential characteristics of the PSF core: $FWHM = 2 a \sqrt{2^{1/b} - 1} = 2.03$

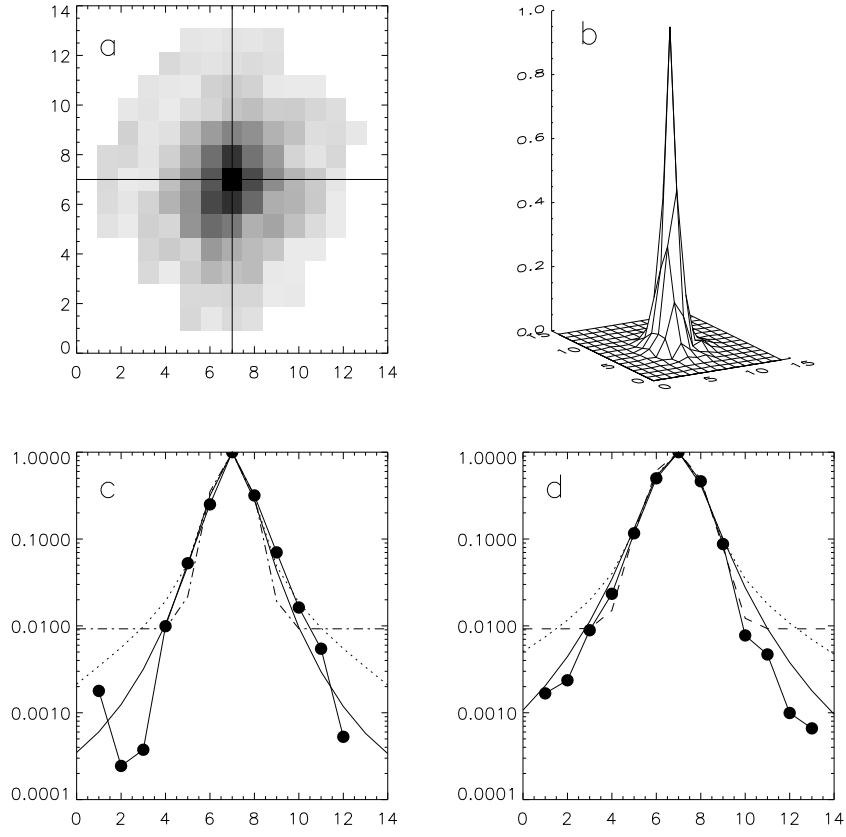


Figure 7. Image of the deconvolved *TRACE* PSF core (a) and its surface plot (b). In (c) and (d) the cross-sections of the peak along the horizontal and vertical lines in (a) core are plotted. The PSF core cross-sections are plotted in thick solid line with black dots. The corresponding cross-sections of the best fits to the core in terms of analytical functions are also overplotted in (c) and (d). The Moffat function fit cross-sections are plotted in a thick solid line, for the Gaussian fit a dash-dotted line is used, and for the fit of the Voigt profile - the dotted line.

pixels and angle of the longer axis of elliptical PSF core deformation $\theta = (1/2) \arctan \varepsilon_y / \varepsilon_x = 70$ degrees counterclockwise to the horizontal edge of the *TRACE* images. The PSF core FWHM determined from Moffat fit is significantly lower than the one derived from Gaussian fit. Our Gaussian core approximation gave FWHM of 2.27 pixels - a result fairly consistent with the mentioned above previous findings (Golub et al., 1999), where also Gaussian characterization of the PSF core was used.

Having the PSF core well characterized and all the necessary information about the *TRACE* diffraction pattern one can reconstruct the entire *TRACE* PSF from solar spectra (see Section 2) and investigate the dependence of PSF geometry on the incident spectrum properties. It is clear that for significantly different spectra the shape of the PSF diffraction maxima must be substantially different in particular for higher diffraction orders.

One of the major factors which determines spectral intensities of radiating plasma is its temperature either in continuum or lines. Especially, line emission intensities are very sensitive to temperature changes. Hence, PSF diffraction maxima shape should vary significantly with

Table I. Parameters of the best elliptical Moffat fit to the *TRACE* PSF core.

a	b	c	x_c	y_c	ε_x	ε_y	bg
1.7405	2.3652	0.2114	-0.0518	-0.1100	-0.4520	0.3773	2.14×10^{-5}

temperature. Therefore, in the next section we study the temperature dependence of PSF shape for a selected temperature range. Possible applications of the PSF properties for determining plasma temperature are discussed as well.

4. Temperature dependence of *TRACE* PSF pattern

We used the method for *TRACE* PSF reconstruction described in Section 2 to determine the PSF shape for solar sources in the isothermal approximation.

For a better overview of the entire *TRACE* PSF pattern we made here a number of simulations assuming that the source plasma is isothermal and in the range of 0.5 - 20.0 MK.

In order to determine the isothermal solar spectra illuminating the instrument, a synthetic spectrum was calculated using the CHIANTI atomic physics database². CHIANTI is a freely available, peer reviewed, atomic physics database and software suite that allows a user to model spectral line and continuum emission from 1 Å to 600,000 Å using factors such as temperature, ionization equilibrium and elemental abundances of the plasma as input parameters (Dere et al., 2001; Young et al., 2003). For our initial CHIANTI synthetic spectrum we decided to

² <http://www.damtp.cam.ac.uk/user/astro/chianti/>

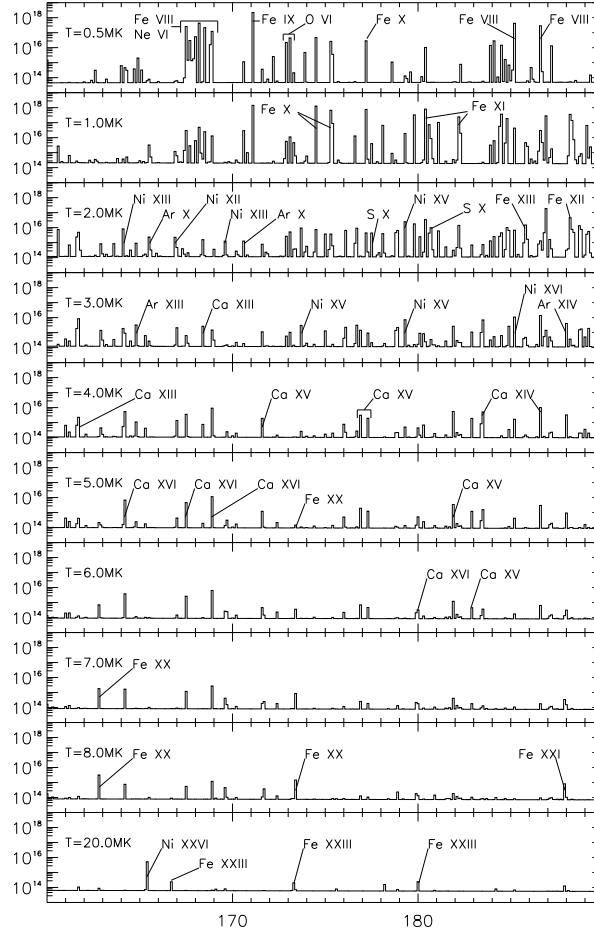


Figure 8. Solar isothermal spectra in the region of *TRACE* 171 Å wavelength window. Plotted are spectra calculated using the *CHIANTI* code for the indicated plasma temperatures.

use the ionization equilibrium calculations of Mazzotta, et al. (Mazzotta, P. et al., 1998) and the solar coronal abundances of Feldman, et al. (Feldman, U. et al., 1992; Allen, C. W., 1973) as our input parameters. The calculated spectra obtained with the *CHIANTI* code are shown in Figure 8. For the lower temperatures in the selected range there is a strong contribution of the line emission seen in the generated spectra superimposed on a relatively flat continuum. With increasing

temperature the line contribution weakens and for temperatures higher than 3.0 MK only a few lines are still pronounced in the spectra. Using the *CHIANTI* package we found that for 0.5 MK the strongest lines come from iron, oxygen and neon. For 1.0 MK the line emission is dominated by iron lines and the continuum radiation reaches the highest level. The radiation from excited nickel and calcium atoms starts to dominate the iron lines at temperatures greater than 2.0 MK. For a few million Kelvin temperatures one can also distinguish stronger lines of ions of nickel, argon and sulfur.

Starting from about 5.0 MK near the middle of the 171 Å *TRACE* filter passband the line emission of strongly ionized iron again increases as the temperature rises and continues to be pronounced towards the higher end of the selected temperature range, up to 20 MK. In order to obtain the contribution of a given solar spectrum to the signal which is measured on the *TRACE* CCD sensor one needs to multiply the spectrum of the incoming radiation by the spectral response curve for the *TRACE* filter in which the image is recorded. The spectral response

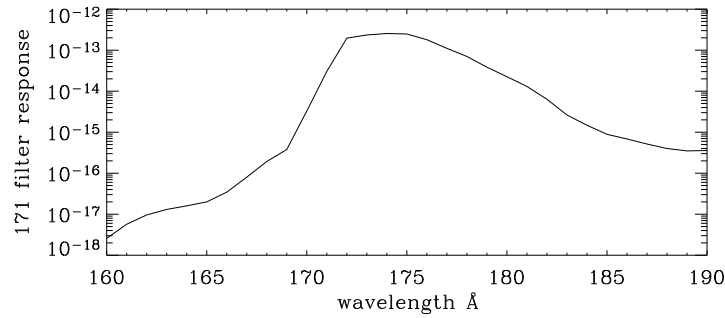


Figure 9. Spectral response curve for the *TRACE* 171 Å filter. The curve is given in units of $\frac{DN/s/pixel}{phot/cm^2/s/sr}$.

curves define how the radiation intensity for any particular wavelength is attenuated by the overall instrument optics. For each of the *TRACE* filters the spectral response curves can be obtained using standard *TRACE* data analysis software. The plot of this curve for the *TRACE* 171 Å channel is shown in Figure 9. The multiplication by the spectral response curve of the 171 Å channel significantly changes the incoming spectrum. The continuum bends and line intensities are modified according to the shape of response curve. The intensities in both band ends are substantially attenuated. The counterparts of the isothermal spectra from Figure 8 multiplied by the spectral response functions of the 171 filter - so called spectral signal contribution functions are

shown in Figure 10. The overall character of the spectra modified by

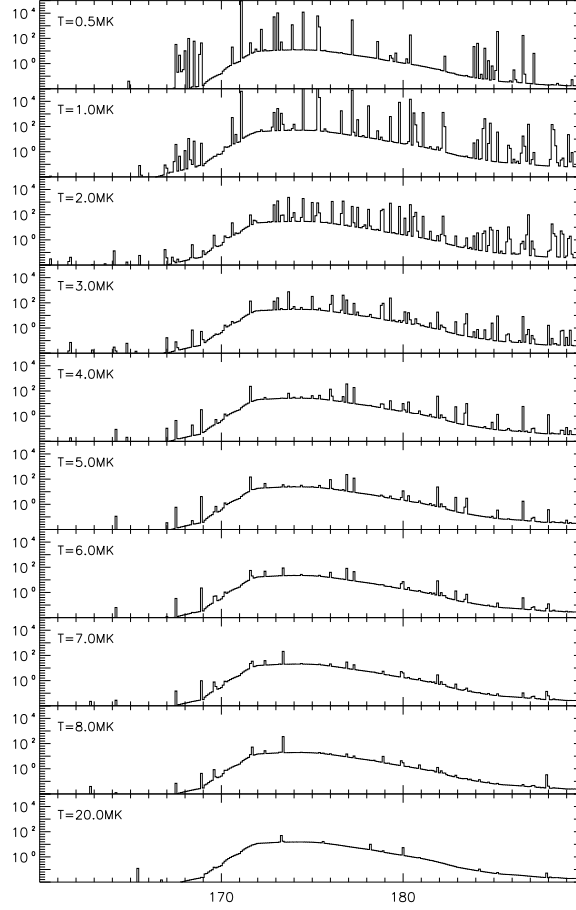


Figure 10. Isothermal spectral contribution functions to the *TRACE* image signal as calculated for the indicated set of temperatures.

the instrument spectral response function does not change substantially in the sense that both lines and continuum are giving substantial contribution to the observed flux. The intense line emission observed for the lower temperature regime flattens almost completely for higher temperatures where the continuum emission with a few stronger lines only becomes the major factor contributing to the observed flux. For lower temperatures, 0.5 MK and 1.0 MK, the lines Fe IX and Fe X ions

dominate the *TRACE* observed spectra. At about 3.0 MK the lines of Ni XV and Ca XV ions start to take over. For higher temperatures around 5 - 6 MK the iron line emission are dominant again this time in lines of Fe XX, Fe XXI, Fe XXII and Fe XXIII ions.

In the next step of our analysis, we consider in more details the dependence of the *TRACE* diffraction pattern on the temperature. We used spectra corrected for 171 Å filter response to construct the *TRACE* PSF shapes in the isothermal approximation. The spectral signal contribution functions shown in Figure 10 were accordingly redistributed over the CCD starting from the CCD center using dispersion equation 4 and the diffraction pattern geometry defined by the angles ϕ_1 , ϕ_2 . Order dependent intensity changes were calculated using equation 2 for each wavelength separately and summed together. Next the resulting diffraction pattern was convolved with the PSF core determined from blind deconvolution to introduce telescope blur and the entire PSF was normalized to the unit integral.

By looking at the modeled PSF surface we observed that individual PSF peak shape depends strongly on the temperature, especially for higher diffraction orders. The variation of *TRACE* PSF pattern with the source plasma temperature is shown in details in Figures 11 and 12. Only the lower order maxima (up to sixth order) keep the form of more or less fuzzy but well defined single compact peaks in the 0.5 - 20.0 MK temperature range analyzed. Over the entire range the temperature variations of higher order diffraction peaks becomes dramatic reflecting a strong dependence of the spectral contribution functions on the source temperature. This dependence of the diffraction pattern on the temperature paves the way for potential use of this effect in detailed mapping of the temperature distribution for flaring kernels.

5. Conclusions

The PSF core for the *TRACE* telescope was deconvolved and fitted with Gaussian, Moffat and Voigt functions. The best fit was obtained with the Moffat function. The Gaussian and Voigt fits gave less accurate parametric characteristics of the core. Both of them are too fuzzy in the off-peak areas.

The deconvolved PSF core is a very sharply peaked and elliptically deformed function. From elliptical Moffat fits we found that the position angle of the longer ellipse axis is 70 degrees and that the core FWHM is 2.03 pixels.

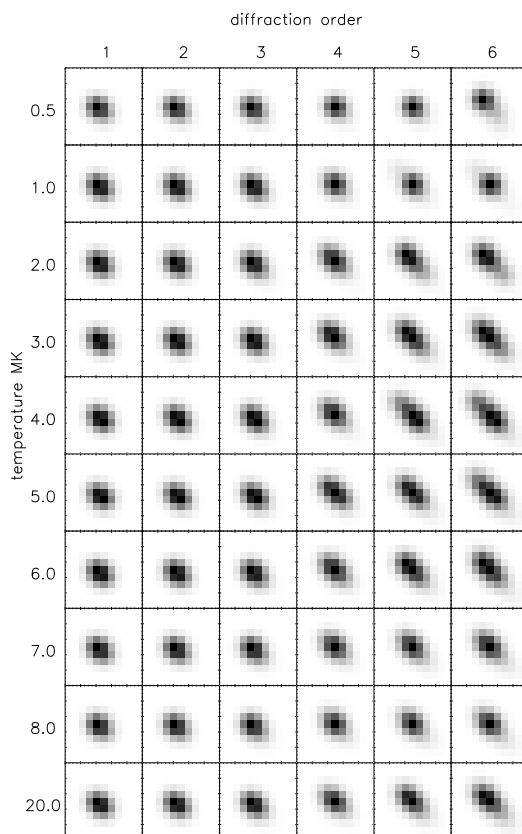


Figure 11. Temperature variability of the individual shape of the *TRACE* PSF diffraction structures (for orders 1 - 6) obtained in the isothermal approximation. Each individual structure was constructed using *CHIANTI* isothermal spectra multiplied by the *TRACE* effective area function, and convolved with the core determined from blind deconvolution. Size of each small panel in this figure is 11×11 *TRACE* pixels.

Deconvolution of *TRACE* images substantially increases the image dynamic range and sharpens the structures seen. The diffraction portion of the PSF can be largely removed from images by deconvolution.

The PSF subordinate diffraction peak shapes and intensities are very sensitive to the temperature as is seen from isothermal modeling of the PSF diffraction pattern. This is particularly important effect influencing the shape and internal structure of the diffraction peaks observed for orders greater than 10. Substantial temperature dependence of the PSF high order diffraction emission suggest that even single *TRACE* images can be used for the analysis of the temperature and

emission measure distribution in the source if the diffraction pattern is of significant strength in the image.

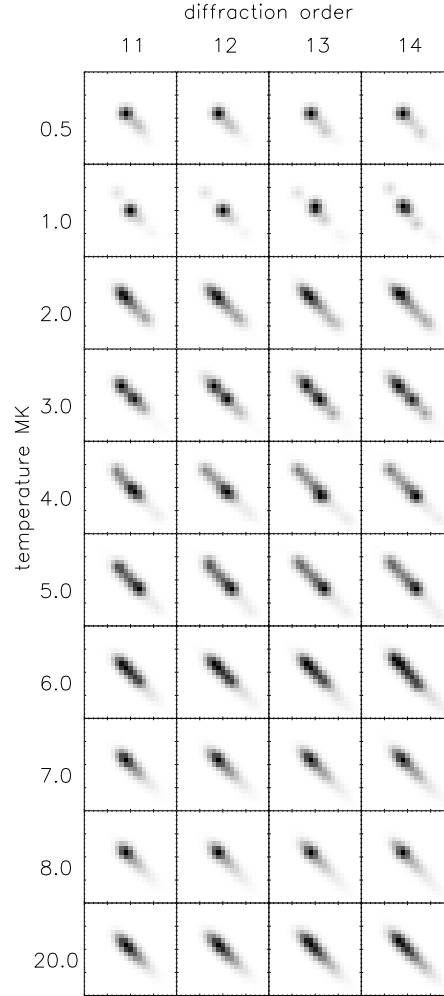


Figure 12. Temperature variability of the individual shape of the *TRACE* PSF diffraction structures (for orders 11 - 14) obtained in the isothermal approximation. Each individual structure was constructed using *CHIANTI* isothermal spectra multiplied by the *TRACE* effective area function, and convolved with the core determined from blind deconvolution. Size of each small panel in this figure is 21×21 *TRACE* pixels.

Acknowledgements

This work has been supported by Polish KBN grant 4T12E 045 29 and NASA grant NAS5-38099 for *TRACE* mission operations and data analysis, through a subcontract of Lockheed-Martin with Montana State University. We thank Dr T. Winter and Dr J. Cirtain for helpful comments and discussion of *CHIANTI* atomic data base properties.

References

- Allen, C. W.:1973, *London: University of London, Athlone Press.*
Ayers and Dainty: 1998, *Optic Letters*, **13**(7), 422.
Dere et al.: 1997, *AASS*, **125**, 149.
Feldman, U. et al.: 1992, *ApJS*, **81**, 387.
Gburek, S.: 2003, *PhD thesis.*
Golub, L. et al.: 1999, *Physics of Plasmas*, **6**, 2205.
Handy et al.: 1999, *Solar Phys.*, **187**, 229.
Lin, A. et al. :2001, *Solar Phys.*, **198**, 385.
Martens, Acton, & Lemen :1995, *Solar Phys.*, **157**, 141.
Mazzotta, P. et al. :1998, *A&AS*, **133**, 403.
Schrijver et al. :1999, *Solar Phys.*, **187**, 26.
Watko, J. A. & Klimchuk, J. A. :2000, *Solar Phys.*, **193**, 77.
Young et al. :2003, *ApJSS*, **144**, 135.

